Studies of Liquid Crystalline Self-Assembly of GdF_3 Nanoplates by In-Plane, Out-of-Plane SAXS

Taejong Paik,[†] Dong-Kyun Ko,[‡] Thomas R. Gordon,[†] Vicky Doan-Nguyen,[‡] and Christopher B. Murray[†,‡,*]

[†]Department of Chemistry, University of Pennsylvania, 231 South 34th Street, Philadelphia, Pennsylvania 19104, United States, and [‡]Department of Materials Science and Engineering, University of Pennsylvania, 3231 Walnut Street, Philadelphia, Pennsylvania 19104, United States

ABSTRACT Directed self-assembly of colloidal nanocrystals into ordered superlattices enables the preparation of novel metamaterials with diverse functionalities. Structural control and precise characterization of these superlattices allow the interactions between individual nanocrystal building blocks and the origin of their collective properties to be understood. Here, we report the directed liquid interfacial assembly of gadolinium trifluoride (GdF_3) nanoplates into liquid crystalline assemblies displaying long-range orientational and positional order. The macroscopic orientation of superlattices is controlled by changing the subphases upon which liquid interfacial assembly occurs. The assembled structures are characterized by a combination of transmission electron microscopy (TEM) and small-angle X-ray scattering (SAXS) measurements performed on a laboratory diffractometer. By doping GdF_3 nanoplates with europium (Eu^{3+}), luminescent phosphorescent superlattices with controlled structure are produced and enable detailed structural and optical characterization.

KEYWORDS: nanocrystals · nanoplates · superlattices · SAXS · liquid crystalline · self-assembly

Assembled nanocrystal superlattices composed of one or more types of nanocrystals have been shown to have novel collective properties.[1−4] Among the vast collection of nanocrystal building blocks, anisotropic nanocrystals offer a new design criterion for tuning assemblies, allowing formation of liquid crystalline phases with differing orientational and positional order.[5,6] Nanorods are well-known anisotropic building blocks which form oriented liquid crystalline superlattices, previously fabricated by drying-mediated self-assembly,[7] electric-field-assisted assembly,[8] depletion attraction,[9] the Langmuir−Blodgett technique,[10] and destabilization by slow diffusion of a nonsolvent.[11] Liquid crystalline assemblies of nanoplates have also been demonstrated.[12−19] Cao *et al*. demonstrated highly ordered assemblies of gadolinium oxide (Gd_2O_3) square nanoplates.[12] However, systematic control of the macroscopic orientation of the superlattice over a large area has remained a challenge.

To understand the origin of the collective interactions between nanocrystals assembled into superlattices, the structure must be precisely characterized. Structural parameters, such as the symmetry, domain orientation, interparticle spacing, and degree of order, all influence the mutual interactions between nanocrystal building blocks.[20−23] Although there are many methods to investigate superlattice structure, small-angle X-ray scattering (SAXS) is one of the best tools because it is a nondestructive method for collecting statistical information over a large area with high accuracy.[2,24] In addition, SAXS offers quantitative information on both the nanocrystals and the assembled superlattices.[25] After assembling nanocrystal superlattices by controlled methods and characterizing the structure with SAXS, the relationship between structure and collective properties can be discerned. This understanding allows us to design the properties of new solids from a set of building blocks, which are distinct from those of individual nanoparticles or molecules.

Grazing-incidence small-angle X-ray scattering (GISAXS) is a powerful method to measure the scattering patterns of periodic nanocrystal superlattices. Two-dimensional area detectors allow for collection of in-plane and out-of-plane scattering from monolayers, multilayers, and binary superlattices.[25−27] High intensity synchrotron radiation sources offer large X-ray scattering intensities with low background and *in situ* capabilities allowing the kinetics of assembly to be studied.[28] However, the accessibility of synchrotron radiation has limited GISAXS use as a more routine structural probe.

Herein, we report directed liquid crystalline assembly of GdF_3 nanoplates by liquid interfacial assembly. Liquid interfacial assembly is a simple, robust, and reproducible

* Address correspondence to cbmurray@sas.upenn.edu.

Received for review August 10, 2011 and accepted September 9, 2011.

Published online September 11, 2011
10.1021/nn203049t

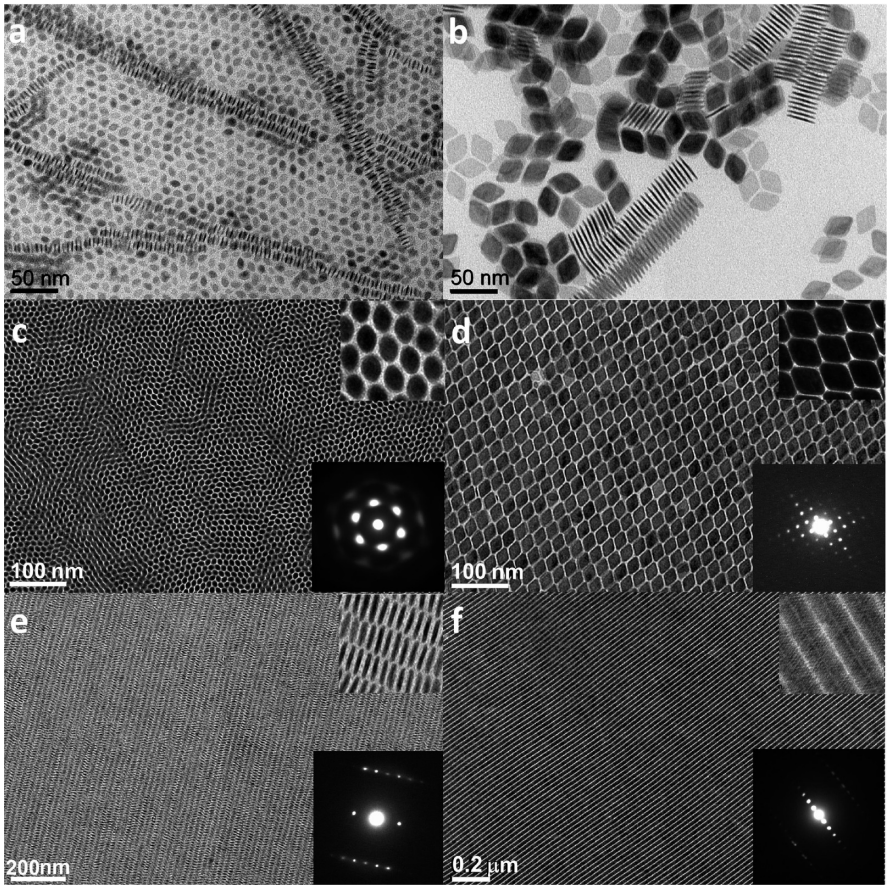

Figure 1. TEM images of (a) ellipsoidal, (b) rhombic nanoplates assembled into (c,d) columnar and (e,f) lamellar liquid crystalline superlattices through a liquid interfacial assembly technique. The top inset is a high-magnification TEM image, and the bottom inset is small-angle electron diffraction pattern.

method to fabricate nanocrystal superlattices.[29−31] We observe that anisotropic GdF_3 nanoplates assemble to form uniform liquid crystalline superlattices with long-range orientational and positional order and demonstrate that liquid crystalline structure is controlled by changing the subphase during the process. Liquid crystalline superlattices are characterized by out-of-plane and in-plane small-angle X-ray scattering techniques with a laboratory X-ray diffractometer. We observed X-ray scattering patterns of oriented films corresponding to characteristic liquid crystalline structures. In addition, phosphorescent superlattices are demonstrated by using europium (Eu^{3+})-doped GdF_3 nanoplates.

RESULTS AND DISCUSSION

GdF_3 nanoplates are chosen as the nanocrystal building blocks because the nanoplates are monodisperse and tunable in shape and size. Ellipsoidal and rhombic GdF_3 nanoplates are synthesized *via* high-temperature colloidal synthesis. Transmission electron microscopy (TEM) images indicate that ellipsoidal nanoplates are 16 nm along the long axis and 10 nm along the short axis (Figure 1a), and rhombic nanoplates are 35 nm along the long axis and 25 nm along short axis (Figure 1b).

Liquid crystalline superlattices are formed using a liquid interfacial assembly and transfer technique, in which a drop of a nanocrystal suspension in a volatile solvent is slowly dried on glycol-type polar subphases in a Teflon well covered with a glass slide, and then the resulting nanocrystal film is transferred to a substrate. Both ellipsoidal and rhombic nanoplates are observed to stack preferentially face-to-face, forming 1-D ordered assemblies (Figure 1a,b). Upon liquid interfacial assembly, edge-to-edge interactions also affect ordering simultaneously, building 3-D close-packed superlattices. Two different liquid crystalline structures are observed in films assembled on the surface of diethylene glycol. In some regions of the superlattice film, nanoplates assemble into columnar liquid crystalline structures, wherein the plates lie flat on the subphase and stack to form columns oriented out-of-plane (Figure 1c for ellipsoidal plates, Figure 1d for rhombic plates). In other regions, ordered lamellar structures are observed, in which the nanoplates assemble by standing edge-on, forming a lamellar liquid crystalline structure parallel to the liquid interface (Figure 1e for ellipsoidal plate, Figure 1f for rhombic plates).

The columnar assembly of ellipsoidal nanoplates shows short-range positional order with quasi-long-range

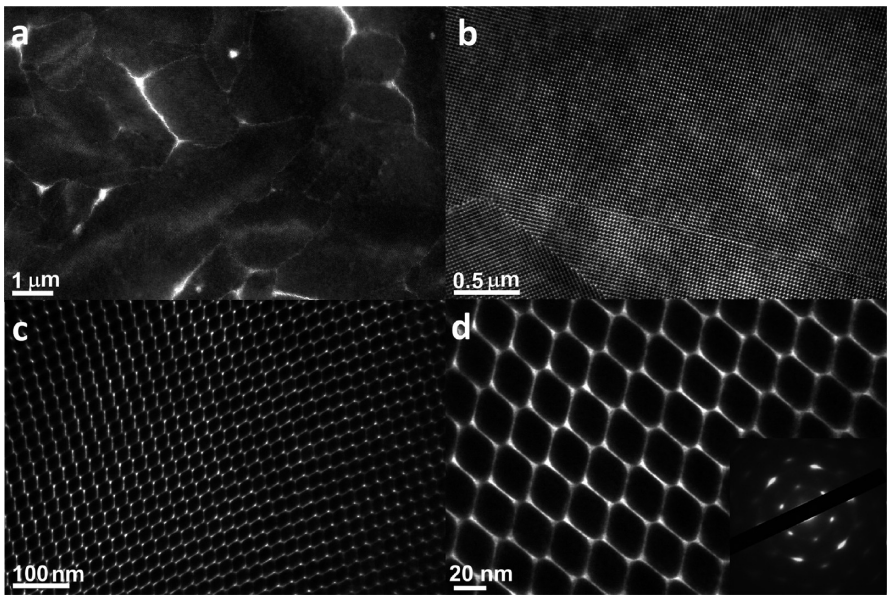

Figure 2. Series of TEM images of columnar liquid crystalline phase domains of rhombic GdF_3 nanoplates from low magnification to high magnification. Bottom inset is a wide-angle electron diffraction pattern.

orientational order (see Figure 1c). A hexagonal small-angle electron diffraction pattern indicates that the phase of the columnar assembly of ellipsoidal nanoplates is hexatic.[32] Locally, the plates' long axes are oriented in the same direction, forming a centered rectangular columnar phase (see Figure 1c inset). Each column reflects the shape of an isolated nanoplate, which indicates that the nanoplates within each column perfectly overlap to maximize the face-to-face interaction. The electron diffraction patterns of columnar assemblies of rhombic nanoplates show two-fold symmetry representing a rectangular columnar liquid crystalline phase (see Figure 1d inset). Electron diffraction patterns for lamellar superlattices of both ellipsoidal and rhombic nanoplates also have two-fold symmetry (see Figure 1e and 1f inset). This is due to the periodicity of the nanoplates stacking face-to-face and the layering of each stack orthogonal to the stacking direction, indicating a smectic liquid crystalline phase (Figure S1 in Supporting Information). Only two sets of diffraction spots are observed even in multilayer superlattices, meaning that all nanoplates are oriented identically in the plane of the substrate.

Liquid crystalline structures with long-range orientational and positional order are observed over large areas (Figures S2 and S3). Figure 2 displays TEM images of columnar superlattices of rhombic nanoplates at increasing magnifications. The low-magnification image in Figure 2a shows that the domain size ranges between 1 and 10 μm^2. The flat edges of rhombic plates enable the nanoplates to be crystallographically oriented as reflected in the wide-angle single crystalline electron diffraction pattern (inset Figure 2d). Diffraction spots were indexed as the {101}, {301}, {002}, and {200} families of planes, which is consistent with the fast Fourier transform (FFT) of the high-resolution TEM (HRTEM) image of an isolated nanoplate (Figure S4). In addition, rhombic nanoplates are observed to pack efficiently by perfect space filling analogous to tiling of building blocks, leaving minimal space except for the ligand bound to the surface.

The lamellar liquid crystalline structures of rhombic nanoplates also exhibit long-range order and characteristic single crystalline electron diffraction patterns (Figure S5). Due to the fact that these films form multilayered structures, scanning electron microscopy (SEM) images are preferential to visualize the surface structure of the nanoplates assembled edge-on (Figure 3b and Figure S6). We observe that the nanoplates are not oriented perpendicular to the substrate but are tilted with respect to the substrate. TEM tilt analysis shows that the nanoplates in the lamellar structure also preserve translational order along the nanoplate stacks (Figure 3c,d). In addition to single component superlattices, binary superlattices in which plates are coassembled with spherical nanocrystals may be formed in the lamellar liquid crystalline structure (Figure 3e,f). TEM images show that the long axis of each nanoplate aligns parallel to the substrate (Figure 3e), and that the spherical 9 nm hexagonal phase sodium gadolinium tetrafluoride (β-$NaGdF_4$) nanocrystals are located in the void between the plate stacks (Figure 3f). This result demonstrates that the long-range ordered lamellar structure of rhombic nanoplates may be used as a dielectric template directing nanocrystals into periodic one-dimensional arrays.

Phosphorescent assemblies can be fabricated by using europium (Eu^{3+})-doped GdF_3 nanoplates. A lanthanide element has a partially filled f electron inner shell that is responsible for its characteristic optical

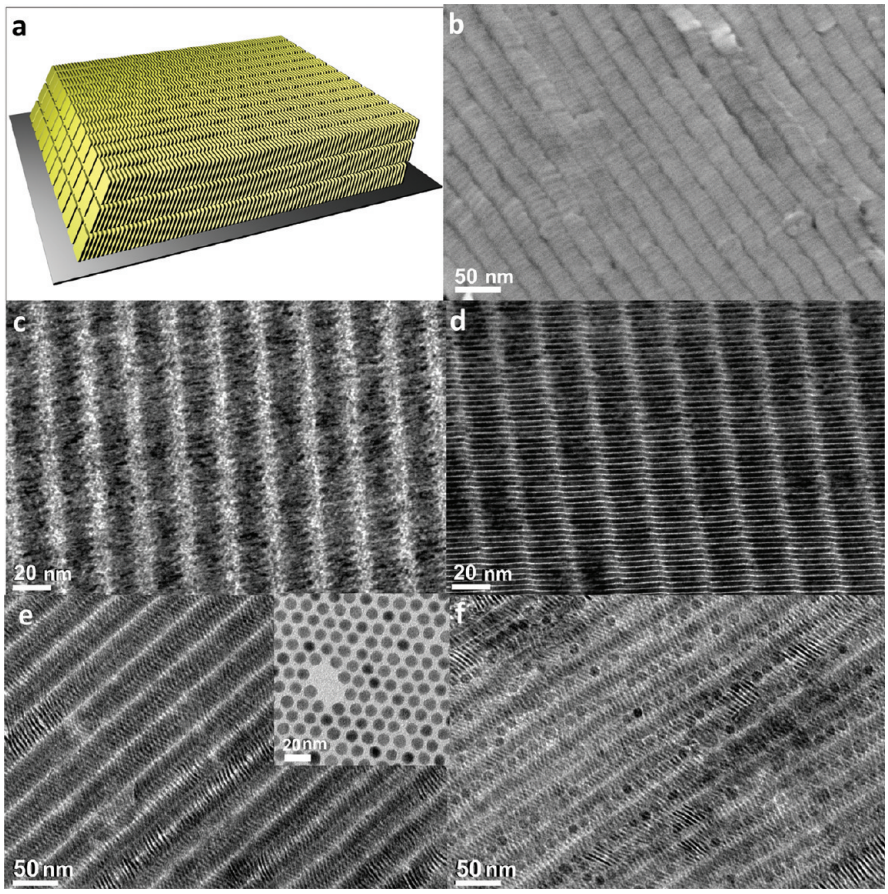

Figure 3. (a) Schematic and (b) SEM image of lamellar liquid crystalline structure of rhombic nanoplates. TEM images of laterally assembled GdF_3 nanoplates collected by tilting the TEM holder from (c) 0° to (d) 53°. TEM images of (e) lamellar liquid crystalline structure and (f) binary superlattices with β-$NaGdF_4$ spherical nanoparticles. Inset in e: TEM image of β-$NaGdF_4$ spherical nanocrystals.

TABLE 1. Intensity Ratio between Emission Peaks of 1% Eu^{3+}-Doped GdF_3 Nanoplates in Defined Structures (Intensity Ratio Is Normalized by the Emission Intensity at 586 nm)

	$^5D_0 \rightarrow {}^7F_0$	$^5D_0 \rightarrow {}^7F_1$		$^5D_0 \rightarrow {}^7F_2$
	$I_{554\ nm}/I_{586\ nm}$	$I_{586\ nm}/I_{586\ nm}$	$I_{592\ nm}/I_{586\ nm}$	$I_{614\ nm}/I_{586\ nm}$
solution	0.14	1	1.49	0.94
drop-casted film	0.18	1	1.58	0.80
columnar assembly	0.15	1	0.96	0.63
lamellar assembly	0.22	1	2.34	0.47

properties. Europium dopant is known as a highly efficient red emitter.[33] We find that the emission spectra of europium-doped GdF_3 nanoplates are perturbed depending on the structure of the liquid crystalline superlattice films (see Table 1). Figure 4 shows the excitation and emission spectrum of 1% Eu^{3+}-doped GdF_3 nanoplates suspended in hexanes, drop-casted onto films, and assembled into the two liquid crystalline superlattices. Characteristic Eu^{3+} red emission which corresponds to $^5D_0 \rightarrow {}^7F_J$ line emissions (J = 0, 1, 2, 3, 4) is observed in all samples. Emission

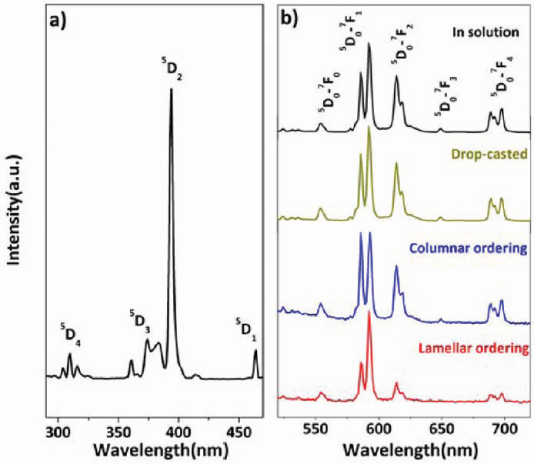

Figure 4. (a) Excitation and (b) emission spectra of 1% Eu^{3+}-doped rhombic GdF_3 nanoplate in solution, in drop-cast film, and liquid crystalline superlattice films measured at room temperature. Excitation wavelength is set as 394 nm, and emission spectra are collected at 90° with a 30° angle between light source and the sample plane (emission spectra are found to be independent of this angle). Excitation spectrum is recorded by monitoring the emission at 592 nm.

spectra obtained from solution and drop-casted films are nearly identical. However, the relative intensities of

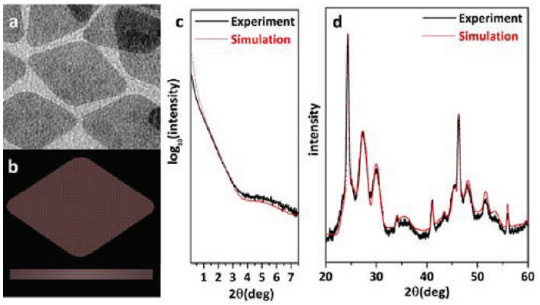

Figure 5. (a) TEM image of rhombic nanoplates used for powder X-ray simulation. (b) Atomistic model generated for simulation. (c) TSAXS and (d) PXRD patterns of rhombic nanoplates; the experimental data (black line) is plotted together with the simulation pattern (red dot) for SAXS and PXRD.

the peaks contributing to the $^5D_0 \rightarrow {}^7F_1$ transition, which is a known magnetic dipole transition, are varied depending on the structure of the assembly. The reason for structure-dependent emission remains unclear. However, the effect of assembly on the optical properties of the film indicates the importance of controlling the formation and precisely characterizing the structure of superlattices, allowing structure–property relationships to be understood and the properties of superlattices to be controlled.

To fully characterize the assembled superlattices, it is essential to first determine the structure of each individual building block. While the width and length of the plates is easily measured by TEM, the thickness of the nanoplates is more difficult to measure due to the tilt in the sample orientation when lying edge-on. Titling experiments conducted on the rhombic nanoplates indicate that the thickness is about 2.4 nm (Figure 3d). To confirm the size and shape of the rhombic nanoplates, powder X-ray diffraction (PXRD) and transmission small-angle X-ray scattering (TSAXS) are simulated based on atomistic models of nanoplates, generated from the statistical analysis of TEM images. The GdF_3 nanoplate models are constructed using the orthorhombic unit cell (JCPDS no. 49-1804).[34] Atomic coordinates and scattering factors are entered into the Debye formula to generate the simulated patterns.[35] A size series of nanocrystals were simulated and entered into a Gaussian dispersion equation, thus introducing a size distribution into simulated patterns. Due to the tendency of the nanoplates to align face-to-face, nanoplates on drop-cast films are found to have a preferred orientation. This results in inaccurate ratios of diffraction intensities in the experimental data. To circumvent this issue, we collect PXRD patterns of concentrated nanocrystal solutions filled in a glass capillary using the Laue geometry, enabling the diffraction patterns to be obtained for randomly oriented nanoplates. Figure 5 shows the TSAXS and PXRD patterns and the simulation results. The input parameters for the simulation are varied to fit the experimental pattern yielding a length of 35 nm, a width of 25 nm, a thickness of 2.4 nm, and a dispersion in the length and width (defined as the standard deviation divided by the mean size) of 8%. The average length and dispersion, determined by measuring the length of 150 nanocrystals in TEM images, are 34.9 nm and 4%, respectively, which is in accordance to the values obtained from X-ray simulation. In PXRD patterns of drop-cast films on a glass substrate, the (101) diffraction peak is overemphasized compared to the nanoplate solution, indicating that the nanoplates preferentially align in the edge-on direction (Figure S7).

After rhombic nanocrystal building blocks are properly characterized, the anisotropic nanocrystal superlattices are investigated using reflection small-angle X-ray scattering (RSAXS) and in-plane small-angle X-ray scattering (in-plane SAXS) measurements on a laboratory X-ray diffractometer equipped with a graded multilayer mirror. The parabolically curved graded multilayer mirror converts the divergent X-ray beam generated from a point source into a parallel beam. This allows a laboratory diffractometer to be used in reflectometry, grazing-incidence, and high-resolution diffractometry with significant improvements in the X-ray intensity.[36] In the RSAXS measurement, X-ray beam scatters off the nanocrystal film on the substrate, as illustrated in Figure 6, and the scattered beam is collected in $\theta/2\theta$ geometry. An offset scan ($\theta + \delta\theta/2\theta$) is performed to avoid strong specular reflection.[37] Bragg diffraction patterns obtained from RSAXS measurements indicate out-of-plane ordering. On the other hand, in-plane SAXS measurements utilize a grazing incident geometry (α_i), and the scattered beam is collected by a scanning detector in a plane parallel to the film surface. In-plane SAXS provides scattering information about in-plane ordering. Therefore, the two scattering measurements are complementary and provide precise structural information to confirm the orientation of the liquid crystalline assemblies.

Figure 6 shows RSAXS and in-plane SAXS results for assemblies of rhombic nanoplates made by liquid interfacial assembly using diethylene glycol as the subphase. Periodicity in the RSAXS and in-plane SAXS patterns indicates that columnar and lamellar phases coexist in the assembled structure. In RSAXS measurements, up to a ninth order of Bragg diffractions is observed with equal spacing that is the result of scattering from the face-to-face ordering of the nanoplates (Figure S8). High-order diffractions indicate that long-range translational order exists within the nanoplate stacks. Peak broadening in SAXS patterns reflects the average domain size of the assembled structure, and an average grain size is calculated using the Scherrer equation.[14,38] SAXS patterns of assembled films are much narrower than those of drop-cast films and are limited by instrumental broadening (Figure S9), indicating that more extensive long-range order is

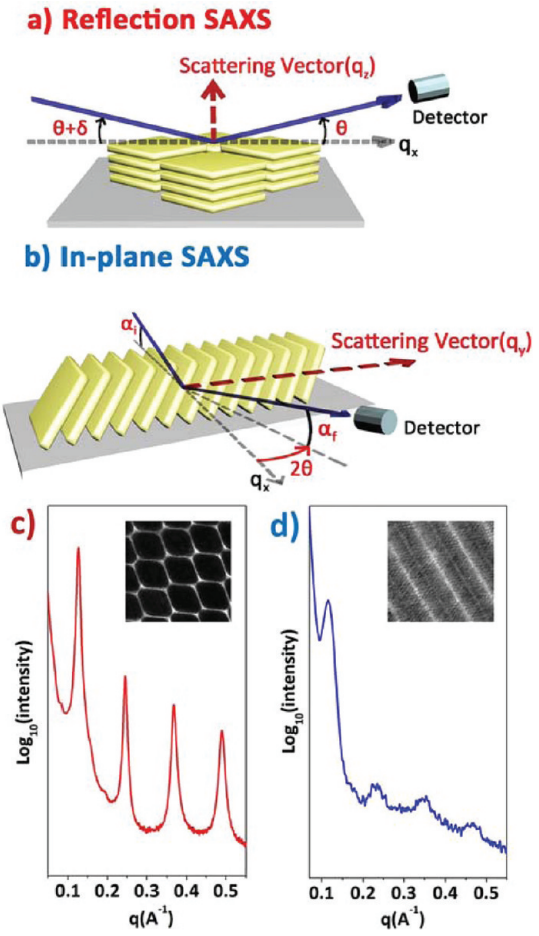

Figure 6. Schematics of a small-angle X-ray scattering experiment. (a) RSAXS), (b) in-plane SAXS, and (c) RSAXS patterns showing fringe patterns corresponding to columnar assembly. (d) In-plane SAXS result indicating lamellar assembly.

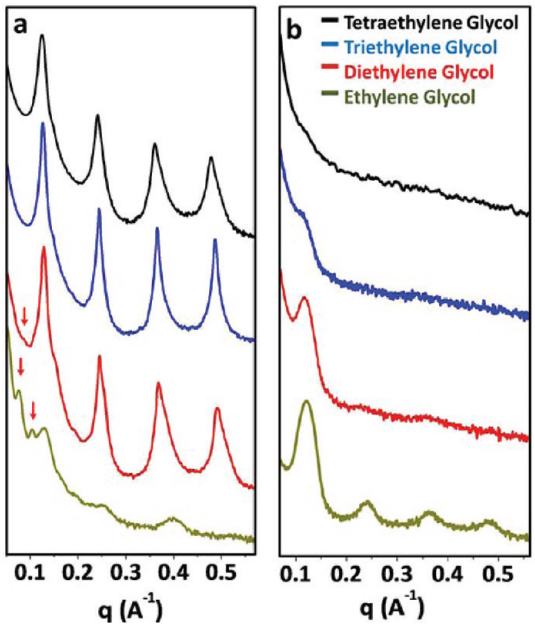

Figure 7. (a) Reflection SAXS and (b) in-plane SAXS measurements of rhombic GdF_3 nanoplate superlattices assembled by liquid interfacial assembly over different subphases. Red arrows indicate diffraction peaks corresponding to 2-D layer ordering of lamellar superlattices.

obtained from liquid interfacial assembly. The average domain size of out-of-plane ordering in columnar assemblies is approximately 0.1 μm, which corresponds to the assembly of 20 nanoplates.

The scattering angles of the peaks in the SAXS pattern are used to determine the average interparticle spacing, where the center-to-center distance between nearest neighbors in the nanoplate stacks is given by $d = 2\pi/q$. In RSAXS, the position of the first diffraction peak is 0.127 A^{-1}, which corresponds to a 4.9 nm of center-to-center distance. Average interparticle spacing is obtained by subtracting the nanoplate thickness from center-to-center distance. The thickness of rhombic nanoplate as calculated by X-ray simulation is 2.4 nm; therefore, the average interparticle spacing in columnar assembled nanoplates is 2.5 nm. Recently, Shevchenko *et al.* reported GISAXS results for 7 nm PbS spherical nanocrystal superlattices.[27] The interparticle spacing of the closed-packed structure was found to be 1.4 nm, which is shorter than those of columnar assembly. It might be expected that the edge of the nanoplates in each columnar stack are intercalated into the void between nanoplates in the next stacks, which increases interparticle spacing (Figure S10). On the other hand, the position of the first diffraction peak from in-plane SAXS is 0.115 A^{-1}, and the lattice spacing in lamellar ordering is 5.5 nm. As described earlier, nanoplates in lamellar assemblies do not lie perpendicular to the substrate but are tilted at an angle of around 50° as measured by TEM tilting analysis (Figure 3c,d). Longer lattice spacing between nanoplates in the lamellar structure may be attributed to the tilt of the nanoplates.

Subphases selected for liquid interfacial assembly play an important role in controlling the macroscopic orientation of superlattices. To confirm a subphase effect, assemblies are produced with samples that have been extensively purified to remove any additional surfactant, avoiding the effects of depletion attraction or change in the surface wetting properties. Four different glycol-type subphases that have different dielectric constants are tested to reveal the subphase effect. RSAXS and in-plane SAXS measurements confirm the trend observed with macroscopic orientation of superlattices (Figure 7). Periodic Bragg peaks in RSAXS are observed on films made over tetraethylene glycol and triethylene glycol subphases. However, in-plane SAXS did not show any characteristic diffraction peaks. This suggests that tetraethylene glycol and triethylene glycol subphases selectively induce the formation of columnar liquid crystalline superlattices as was corroborated by our TEM studies. For ethylene glycol, which has higher dielectric constant than tri- or tetraethylene glycol, the in-plane SAXS result shows

Bragg peaks, while the intensities of Bragg reflections in RSAXS are weaker relative to those of films assembled over less polar subphases. Laterally ordered nanoplates are tilted with respect to the surface. Therefore, out-of-plane order of tilted nanoplate stacks could contribute to produce Bragg diffraction patterns in RSAXS measurement. Multilayers of the 2-D lamellar structure also produce Bragg peaks in the region smaller than the first scattering peak of face-to-face ordering (Figure 7, red arrows). The RSAXS pattern of assembled films over the ethylene glycol clearly shows the Bragg reflections due to layer-by-layer ordering. Results from both RSAXS and in-plane SAXS reveal that lamellar structure is predominant in films assembled over the ethylene glycol subphase. Therefore, the less polar subphases predominantly form columnar superlattices, while more polar subphases tend to form lamellar superlattice structures.

The subphase effect suggests that the assembly in this study is occurring at the liquid−liquid interface rather than the liquid−air interface as has been reported for other systems.[28,39−41] The SAXS results also indicate that the subphase affects the orientation of liquid crystalline superlattices due to the change of dielectric constants because the subphases used for assemblies have similar values of surface tensions but vary in dielectric constant (see Table S1 in the Supporting Information). In the TEM image of columnar assembly, we observed that the superlattice is assembled from the first monolayer and extended to multilayers (Figure S11). Facets of nanoplates are covered by oleic acid, which makes the facets hydrophobic. Therefore, nanoplates on the first layer, which directly contact the subphase, could tend to stand edge-on relative to the polar subphase. On less polar subphases, such as tri- and tetraethylene glycol, the nanoplates lie flat with their faces directly in contact with the subphase. This is similar to previously reported trends of nanorod alignment in the formation of liquid crystalline superlattices.[7,42] After formation of the first layer on the subphase, strong face-to-face interaction between nanoplates can induce self-ordering to overlap facets and build 3-D liquid crystalline superlattices by matching orientation of plates.[43]

To further understand the influence of subphase on superlattice formation, we perform the nanoplates' assemblies without covering the solution container to facilitate faster drying of hexane. It is known that assemblies occur at the liquid−air interface rather than at the liquid−liquid interface under fast drying conditions.[28,39] Therefore, assemblies would not be affected by the subphase. We observe that domain orientations in assembled films are independent of variation of subphases and that the nanoplates lie flat on the substrate. This result supports the idea that the liquid crystalline structure formed by liquid interfacial assembly can be directed by subphases when assemblies occur on the subphases.

CONCLUSION

We demonstrate that columnar and lamellar liquid crystalline superlattices of GdF_3 nanoplates are achieved by liquid interfacial assembly with long-range orientational and positional order. The choice of subphase is found to be an important factor in directing the orientation of the superlattices, where a more polar subphase favors lamellar liquid crystalline structure and a less polar subphase favors columnar liquid crystalline assemblies of GdF_3 nanoplates. The structure was characterized by RSAXS and in-plane SAXS using a laboratory X-ray diffractometer. Characteristic fringe scattering patterns in RSAXS and in-plane SAXS confirm this subphase effect. Furthermore, we identify structure-dependent optical properties of assembled Eu^{3+}-doped GdF_3 nanoplates.

MATERIALS AND METHODS

Materials. All chemicals were used as purchased without any further purification. Gadolinium(III) oxide (99.99%), oleic acid (technical grade, 90%), 1-octadecene (technical grade, 90%), and lithium fluoride (99.98%) were purchased from Sigma Aldrich. Trifluoroacetic acid (99.5+%) was purchased from Alfa Aesar. Gadolinium trifluoroacetate precursors were prepared with the literature method using gadolinium(III) oxide and trifluoroacetic acid as reactants.[44] Ethylene glycol (99.5%), diethylene glycol (99%), triethylene glycol (99%), and tetraethylene glycol (99.5%) were purchased from Acros Organics.

Synthesis of GdF_3 Nanoplates. Two millimolar of gadolinium trifluoroacetate and 6 mmol of lithium fluoride were added to a 125 mL three-neck flask containing 30 mL of oleic acid and 30 mL of 1-octadecene. This solution was degassed at 125 °C for 1 h. Then, the solution was heated to 290 °C under N_2 environment at a rate of 10 °C/min and maintained at this temperature for an hour (ellipsoidal plate) or for 4 h (rhombic plate). Lithium ions were not incorporated into the nanoplates, but the amount of lithium fluoride added was adjusted to control the morphology and size of nanoplates. Purification was conducted by adding excess ethanol and centrifugation. GdF_3 nanoplates were redissolved in hexane, chloroform, or toluene. Residual lithium fluoride, which is insoluble in nonpolar solvents, was simply removed by centrifugation.

Synthesis of β-$NaGdF_4$ Spherical Nanoparticles. The synthetic procedure was the same as the method used for GdF_3 nanoplates, except that 4 mmol of sodium fluoride was used instead of lithium fluoride. The reaction was done at 290 °C for 5 h.

Liquid Crystalline Assembly of GdF_3 Nanoplates. The assembly process follows the procedure developed in ref 28. First, a Teflon well was filled with glycol-type subphases. Then, 30 μL of the nanoplates solution (concentration is about 20 mg/mL) was added on top of the surface of the subphase. The Teflon well was covered with a glass slide to allow the slow drying of hexane. Once the nanoplate membrane was formed, films were transferred to carbon-coated TEM grids for microscopic analysis or a SiO_2/Si wafer for RSAXS and in-plane SAXS analysis. Further drying was performed in a vacuum chamber to remove residual subphase solvent.

X-ray Diffraction Simulation. Atomistic models of GdF_3 nanocrystals were first constructed using Materials Studio 4.4.[34] The X-ray diffraction intensity, $I(q)$, was calculated using Debye equations[35]

$$I(q) = I_0 \sum_m \sum_n F_m F_n \frac{\sin(qr_{mn})}{(qr_{mn})}$$

where I_0 is the incident intensity, $q = 4\pi \sin\theta/\lambda$ is the scattering parameter for X-rays of wavelength λ, diffracted through the angle θ, and r_{mn} is the distance between atoms m and n, with atomic form factors F_m and F_n, respectively. Atomic form factors were calculated from tabulated Cromer–Mann coefficients. The Debye equation was discretized by binning identical distances to give the following equation to reduce calculation time[45]

$$I(q) = \frac{I_0}{q} \sum_m \sum_n F_m F_n \frac{\rho(r_{mn})}{r_{mn}} \sin(qr_{mn})$$

where $\rho(r_{mn})$ is the multiplicity of each unique distance (r_{mn}) in the structure.

Structure Characterization. TEM images and electron diffraction patterns were recorded using a JEM-1400 microscope equipped with a SC1000 ORIUS CCD camera operating at 120 kV. Scanning electron microscopy (SEM) was performed on a JEOL 7500F HRSEM. RSAXS, in-plane SAXS, and powder X-ray diffraction were measured using a Rigaku Smartlab high-resolution diffractometer equipped with a 2.2 kW sealed tube generator. The X-ray beam (Cu Kα radiation, $\lambda = 1.54056$ Å) was collimated as a parallel beam by parabolically curved multilayer mirrors placed in front of the sample. The beam dimension was 0.05 mm × 5 mm (height × width) for both measurements. The offset angle was obtained by performing a series of omega scans, while the detector was fixed in place. Three omega scans were performed by varying the 2θ position (0.8, 1.2, 1.5°), and the offset angle was determined from the collected profiles automatically by the software, which was about 0.1°. For in-plane SAXS measurement, incident angle (α_i) of the X-ray beam was chosen as 0.3°. Photoluminescence measurements were performed with a Jobin Yvon Fluorolog-3 fluorimeter.

Acknowledgment. T.-J.P. was supported by the Office of Naval Research, MURI W911NF-08-1-0364. The National Science Foundation supported D.-K.K. though PENN MRSEC DMR-0520020 and T.R.G. through the Nano/Bio Interface Center at the University of Pennsylvania Grant Number DMR08-32802. V. D.-N.'s X-ray modeling was supported by the Department of Energy's Advanced Research Projects Agency, Energy (ARPA-E) DE-AR0000123. C.B.M. is grateful for the support of the Richard Perry University Professorship.

Supporting Information Available: Low-magnification TEM and SEM images of assemblies, HRTEM images and FFT patterns of rhombic GdF_3 nanoplates, RSAXS and in-plane SAXS profiles of assemblies, physical properties of the subphases. This material is available free of charge *via* the Internet at http://pubs.acs.org.

REFERENCES AND NOTES

1. Murray, C. B.; Kagan, C. R.; Bawendi, M. G. Synthesis and Characterization of Monodisperse Nanocrystals and Close-Packed Nanocrystal Assemblies. *Annu. Rev. Mater. Sci.* **2000**, *30*, 545–610.
2. Murray, C. B.; Kagan, C. R.; Bawendi, M. G. Self-Organization of CdSe Nanocrystallites into Three-Dimensional Quantum Dot Superlattices. *Science* **1995**, *270*, 1335–1338.
3. Collier, C. P.; Vossmeyer, T.; Heath, J. R. Nanocrystal Superlattices. *Annu. Rev. Phys. Chem.* **1998**, *49*, 371–404.
4. Urban, J. J.; Talapin, D. V.; Shevchenko, E. V.; Kagan, C. R.; Murray, C. B. Synergism in Binary Nanocrystal Superlattices Leads to Enhanced p-Type Conductivity in Self-Assembled PbTe/Ag_2Te Thin Films. *Nat. Mater.* **2007**, *6*, 115–121.
5. Gabriel, J.-C. P.; Davidson, P. Mineral Liquid Crystals from Self-Assembly of Anisotropic Nanosystems. *Top. Curr. Chem.* **2003**, *226*, 119–172.
6. Murphy, C. J.; Sau, T. K.; Gole, A. M.; Orendorff, C. J.; Gao, J.; Gou, L.; Hunyadi, S. E.; Li, T. Anisotropic Metal Nanoparticles: Synthesis, Assembly, and Optical Applications. *J. Phys. Chem. B* **2005**, *109*, 13857–13870.
7. Baker, J. L.; Widmer-Cooper, A.; Toney, M. F.; Geissler, P. L.; Alivisatos, A. P. Device-Scale Perpendicular Alignment of Colloidal Nanorods. *Nano Lett.* **2010**, *10*, 195–201.
8. Ryan, K. M.; Mastroianni, A.; Stancil, K. A.; Liu, H.; Alivisatos, A. P. Electric-Field-Assisted Assembly of Perpendicularly Oriented Nanorod Superlattices. *Nano Lett.* **2006**, *6*, 1479–1482.
9. Baranov, D.; Fiore, A.; van Huis, M.; Giannini, C.; Falqui, A.; Lafont, U.; Zandbergen, H.; Zanella, M.; Cingolani, R.; Manna, L. Assembly of Colloidal Semiconductor Nanorods in Solution by Depletion Attraction. *Nano Lett.* **2010**, *10*, 743–749.
10. Kim, F.; Kwan, S.; Akana, J.; Yang, P. Langmuir–Blodgett Nanorod Assembly. *J. Am. Chem. Soc.* **2001**, *123*, 4360–4361.
11. Talapin, D. V.; Shevchenko, E. V.; Murray, C. B.; Kornowski, A.; Förster, S.; Weller, H. CdSe and CdSe/CdS Nanorod Solids. *J. Am. Chem. Soc.* **2004**, *126*, 12984–12988.
12. Cao, Y. C. Synthesis of Square Gadolinium-Oxide Nanoplates. *J. Am. Chem. Soc.* **2004**, *126*, 7456–7457.
13. Zhang, Y.-W.; Sun, X.; Si, R.; You, L.-P.; Yan, C.-H. Single-Crystalline and Monodisperse LaF_3 Triangular Nanoplates from a Single-Source Precursor. *J. Am. Chem. Soc.* **2005**, *127*, 3260–3261.
14. Saunders, A. E.; Ghezelbash, A.; Smilgies, D.-M.; Sigman, M. B., Jr.; Korgel, B. A. Columnar Self-Assembly of Colloidal Nanodisks. *Nano Lett.* **2006**, *6*, 2959–2963.
15. Sun, X.; Zhang, Y.-W.; Du, Y.-P.; Yan, Z.-G.; Si, R.; You, L.-P.; Yan, C.-H. From Trifluoroacetate Complex Precursors to Monodisperse Rare-Earth Fluoride and Oxyfluoride Nanocrystals with Diverse Shapes through Controlled Fluorination in Solution Phase. *Chem.—Eur. J.* **2006**, *13*, 2320.
16. Yu, T.; Joo, J.; Park, Y. I.; Hyeon, T. Single Unit Cell Thick Samaria Nanowires and Nanoplates. *J. Am. Chem. Soc.* **2006**, *128*, 1786–1787.
17. Kooij, F. M.; v., d.; Kassapidou, K.; Lekkerkerker, H. N. W. Liquid Crystal Phase Transitions in Suspensions of Polydisperse Plate-like Particles. *Nature* **2000**, *406*, 868–871.
18. Zhuang, Z.; Peng, Q.; Zhang, B.; Li, Y. Controllable Synthesis of Cu_2S Nanocrystals and Their Assembly into a Superlattice. *J. Am. Chem. Soc.* **2008**, *130*, 10482–10483.
19. Huo, Z.; Tsung, C.-K.; Huang, W.; Fardy, M.; Yan, R.; Zhang, X.; Li, Y.; Yang, P. Self-Organized Ultrathin Oxide Nanocrystals. *Nano Lett.* **2009**, *9*, 1260–1264.
20. Chen, J.; Dong, A.; Cai, J.; Ye, X.; Kang, Y.; Kikkawa, J. M.; Murray, C. B. Collective Dipolar Interactions in Self-Assembled Magnetic Binary Nanocrystal Superlattice Membranes. *Nano Lett.* **2010**, *10*, 5103–5108.
21. Sun, B.; Sirringhaus, H. Surface Tension and Fluid Flow Driven Self-Assembly of Ordered ZnO Nanorod Films for High-Performance Field Effect Transistors. *J. Am. Chem. Soc.* **2006**, *128*, 16231–16237.
22. Koleilat, G. I.; Levina, L.; Shukla, H.; Myrskog, S. H.; Hinds, S.; Pattantyus-Abraham, A. G.; Sargent, E. H. Efficient, Stable Infrared Photovoltaics Based on Solution-Cast Colloidal Quantum Dots. *ACS Nano* **2008**, *2*, 833–840.
23. Talapin, D. V.; Murray, C. B. PbSe Nanocrystal Solids for n- and p-Channel Thin Film Field-Effect Transistors. *Science* **2005**, *310*, 86–89.
24. Korgel, B. A.; Fullam, S.; Connolly, S.; Fitzmaurice, D. Assembly and Self-Organization of Silver Nanocrystal Superlattices: Ordered "Soft Spheres". *J. Phys. Chem. B* **1998**, *102*, 8379–8388.
25. Heitsch, A. T.; Patel, R. N.; Goodfellow, B. W.; Smilgies, D.-M.; Korgel, B. A. GISAXS Characterization of Order in Hexagonal Monolayers of FePt Nanocrystals. *J. Phys. Chem. B* **2010**, *114*, 14427–14432.
26. Smith, D. K.; Goodfellow, B.; Smilgies, D.-M.; Korgel, B. A. Self-Assembled Simple Hexagonal AB_2 Binary Nanocrystal Superlattices: SEM, GISAXS, and Defects. *J. Am. Chem. Soc.* **2009**, *131*, 3281–3290.

27. Lee, B.; Podsiadlo, P.; Rupich, S.; Talapin, D. V.; Rajh, T.; Shevchenko, E. V. Comparison of Structural Behavior of Nanocrystals in Randomly Packed Films and Long-Range Ordered Superlattices by Time-Resolved Small Angle X-ray Scattering. *J. Am. Chem. Soc.* **2009**, *131*, 16386–16388.
28. Narayanan, S.; Wang, J.; Lin, X.-M. Dynamical Self-Assembly of Nanocrystal Superlattices during Colloidal Droplet Evaporation by *In Situ* Small Angle X-ray Scattering. *Phys. Rev. Lett.* **2004**, *93*, 135503.
29. Dong, A.; Chen, J.; Vora, P. M.; Kikkawa, J. M.; Murray, C. B. Binary Nanocrystal Superlattice Membranes Self-Assembled at the Liquid–Air Interface. *Nature* **2010**, *466*, 474–477.
30. Dong, A.; Ye, X.; Chen, J.; Murray, C. B. Two-Dimensional Binary and Ternary Nanocrystal Superlattices: The Case of Monolayers and Bilayers. *Nano Lett.* **2011**, *11*, 1804–1809.
31. Ye, X.; Collins, J. E.; Kang, Y.; Chen, J.; Chen, D. T. N.; Yodh, A. G.; Murray, C. B. Morphologically Controlled Synthesis of Colloidal Upconversion Nanophosphors and Their Shape-Directed Self-Assembly. *Proc. Natl. Acad. Sci. U.S.A.* **2010**, *107*, 22430–22435.
32. Chaikin, P. M.; Lubensky, T. C. *Principles of Condensed Matter Physics*; Cambridge University Press: Cambridge, UK, 1995.
33. Wegh, R. T.; Donker, H.; Oskam, K. D.; Meijerink, A. Visible Quantum Cutting in $LiGdF_4:Eu^{3+}$ through Downconversion. *Science* **1999**, *283*, 663–666.
34. Zalkin, A.; Templeton, D. H. The Crystal Structures of YF_3 and Related Compounds. *J. Am. Chem. Soc.* **1953**, *75*, 2453–2458.
35. Murray, C. B.; Norris, D. J.; Bawendi, M. G. Synthesis and Characterization of Nearly Monodisperse CdE (E = Sulfur, Selenium, Tellurium) Semiconductor Nanocrystallites. *J. Am. Chem. Soc.* **1993**, *115*, 8706–8715.
36. Schuster, M.; Gobel, H. Parallel-Beam Coupling into Channel-Cut Monochromators Using Curved Graded Multilayers. *J. Phys. D: Appl. Phys.* **1995**, *28*, A270–A275.
37. Omote, K.; Ito, Y.; Kawamura, S. Small Angle X-ray Scattering for Measuring Pore-Size Distributions in Porous Low-κ Films. *Appl. Phys. Lett.* **2003**, *82*, 544–546.
38. Smilgies, D.-M. Scherrer Grain-Size Analysis Adapted to Grazing-Incidence Scattering with Area Detectors. *J. Appl. Crystallogr.* **2009**, *42*, 1030–1034.
39. Bigioni, T. P.; Lin, X.-M.; Nguyen, T. T.; Corwin, E. I.; Witten, T. A.; Jaeger, H. M. Kinetically Driven Self-Assembly of Highly Ordered Nanoparticle Monolayers. *Nature* **2006**, *5*, 265–270.
40. Friedrich, H.; Gommes, C. J.; Overgaag, K.; Meeldijk, J. D.; Evers, W. H.; de Nijs, B.; Boneschanscher, M. P.; de Jongh, P. E.; Verkleij, A. J.; de Jong, K. P.; van Blaaderen, A.; Vanmaekelbergh, D. Quantitative Structural Analysis of Binary Nanocrystal Superlattices by Electron Tomography. *Nano Lett.* **2009**, *9*, 2719–2724.
41. Bodnarchuk, M. I.; Kovalenko, M. V.; Pichler, S.; Fritz-Popovski, G.; Hesser, G.; Heiss, W. Large-Area Ordered Superlattices from Magnetic Wustite/Cobalt Ferrite Core/Shell Nanocrystals by Doctor Blade Casting. *ACS Nano* **2010**, *4*, 423–431.
42. Titov, A. V.; Kral, P. Modeling the Self-Assembly of Colloidal Nanorod Superlattices. *Nano Lett.* **2008**, *8*, 3605–3612.
43. Maeda, H.; Maeda, Y. Liquid Crystal Formation in Suspensions of Hard Rodlike Colloidal Particles: Direct Observation of Particle Arrangement and Self-Ordering Behavior. *Phys. Rev. Lett.* **2003**, *90*, 018303.
44. Roberts, J. E. Lanthanum and Neodymium Salts of Trifluoroacetic Acid. *J. Am. Chem. Soc.* **1961**, *83*, 1087–1088.
45. Hall, B. D.; Monot, R. Calculating the Debye–Scherrer Diffraction Pattern for Large Clusters. *Comp. Phys.* **1991**, *5*, 414.